

## **Fluid Dynamics of Thin Steel Slab Continuous Casting Secondary Cooling Zone Air Mists**

J.I. Minchaca M., A.H. Castillejos E.\*, F.A. Acosta G. and S. Murphy<sup>1</sup>  
Centre for Research and Advanced Studies, CINVESTAV - Unidad Saltillo  
Carr. Saltillo-Monterrey Km. 13.5, Ramos Arizpe, Coahuila, Mexico

<sup>1</sup>Oxford Lasers Ltd.

Unit 8, Moorbrook Park, Didcot, Oxon, OX11 7HP, UK

### **Abstract**

Spray cooling technology plays a prominent role in the secondary cooling of continuously cast thin steel slabs. The prevailing cooling conditions arise from the nature of the intermittent contact of drops with the hot metallic surface, which is affected primarily by the size, velocity and water flux of the drops approaching the surface. This study reports laboratory and computational work carried out to determine these properties for air-mist jets generated by two different fan nozzles, operating over a wide range of water and air flow rates and pressures. A Particle/Droplet Image Analysis (PDIA) technique was used to measure simultaneously the droplet size and velocity spectra and their correlation. Room temperature measurements were carried out over small probe volumes adjacent and perpendicular to the plane where the steel strand would stand in the actual process. Furthermore, the distributions of impacting water flux and mist impact pressure were measured to obtain a fuller characterization of the mists. On the theoretical side, a computational fluid-dynamic (CFD) model based on the solution of the 3-D turbulent Navier-Stokes equation for the air coupled to the motion equation for the water drops was used for predicting the mist dynamics. The model requires exclusively the design and operating characteristics of the particular nozzle and its corresponding drop-size distribution. The PDIA measurements showed that the number and volume distributions of droplet size followed log-normal and Nukiyama-Tanasawa distributions, respectively. Additionally, the distributions were correlated well to the water- and air-nozzle pressures over the wide range of conditions studied. Input of these results to the CFD model led to an excellent prediction of the mist dynamics, as the extensive validation results demonstrated. The increase in the proportion of finer and faster drops that was found with the increase in air-nozzle pressure for a given water flow rate, suggests that the intensification in boiling heat transfer reported in other studies, may be related to a more frequent and intimate contact of finer drops with the surface.

---

\*Corresponding Author:  
humberto.castillejos@cinvestav.edu.mx

## Introduction

Spray cooling technology plays a prominent role in the secondary cooling of continuously cast steel, removing on average  $\sim 60\%$  of the total thermal energy contained in Compact Strip Processing (CSP) thin slabs [1]. The cooling by sprays or air-mists is controllable through the selection of nozzle type, nozzle operating conditions and nozzle position with respect to the strand. These features make water spray and air-mists ideally suited for controlling the heat extraction distribution from the strand surface, with the objectives of achieving optimum levels of quality and productivity. In a typical CSP machine, the nozzle types and positions are fixed and the only degrees of freedom for the operator are the operating conditions, i.e., the water flow rate in the case of hydraulic nozzles and the water- and air-flow rates and pressures in pneumatic ones. In the case of pneumatic nozzles, heat transfer experiments have shown that for a given water flow rate, intensified cooling conditions can be achieved by increasing the air-nozzle pressure,  $p_a$ , to maintain the air-to-water flow rates ratio,  $A/W \geq 10$  [2], [3]. These findings have been demonstrated in practice by showing that a judicious control of the operating conditions of pneumatic nozzles increases the productivity of CSP casters, without detriment in the quality of the product [3], [4]. However, more information is required to determine how the spray parameters (droplet size,  $d_d$ , droplet velocity,  $u$ , and water flux,  $w$ ) vary with the operating conditions and how they affect the heat transfer phenomena, particularly in the film boiling and transition boiling regimes. Given the large number of parameters and their combinations affecting the spray characteristics, the number of necessary experiments would be enormous unless studies center in understanding the governing mechanisms of this complex process. The objective of the work described in this paper was to gain fundamental understanding about the fluid dynamics of industrial air mists used in thin slab continuous casting.

Pedersen [5] used droplets with diameters ranging from 200 to 400  $\mu\text{m}$  and approach velocities from 2.4 to 10 m/s, impinging on heated surfaces at temperatures from 100 to 982  $^\circ\text{C}$  to investigate the dynamic behavior and heat transfer characteristics of individual water droplets. The author suggested that the transition from wetting to non-wetting impact of individual droplets was affected by the impact velocity of the droplets, i.e., that the Leidenfrost temperature was influenced by the dynamic behavior of the droplets. Also, it was reported that in the film boiling or non-wetting regime, the effectiveness of heat transfer (i.e., the fraction of heat

taken by the liquid with respect to the theoretical maximum for complete evaporation on the surface) increased by increasing the approach velocity of the droplet. This behavior has been taken as an indication of the relationship between the heat transfer process and the droplet deformation behavior during impact [6]. It is generally agreed that the Weber number ( $We_{zs} = \rho_d u_{zs}^2 d_d / \sigma$ ) associated to the normal collision velocity, characterizes the impact or deformation mode of the drops [6], [7]. Also, the angle of the droplet trajectory with respect to the hot surface has been found to affect the Leidenfrost temperature [8]. According to the investigators [8], small impinging angles ( $< 45^\circ$ ) reduce the Leidenfrost temperature because the large tangential velocity decreases the chance of physical contact between the drop and the surface and in this condition, the gas boundary layer is likely to be important. Bernardin et al. [9] reported that the  $We_{zs}$  has a strong influence on the spreading characteristics and integrity of droplets. In the film boiling regime and at low impact Weber numbers ( $We_{zs} < 20$ ) the authors found that the surface tension force preserves the integrity of the drop, which rebounds complete after impact. But, as the  $We_{zs}$  becomes larger the spread time of the drops diminishes and the instabilities responsible for their break-up augment. This behavior was observed in all boiling regimes, i.e., film boiling, transition boiling and nucleation boiling. A recent study investigated the effect of the heat transfer mechanism on the secondary atomization of millimetric water droplets, impacting on a surface at different velocities [10]. It was found that a larger kinetic energy at impingement caused a larger spreading of the liquid lamella which resulted in smaller thicknesses and eventually in finer secondary droplets once the lamella ruptured. Another observation widely reported [10] was the formation of a central jet whose height increased as the impact velocity became larger.

The effect of droplet parameters in multi-drop systems (sprays) on the impaction and heat transfer phenomena has been investigated in several works [11]-[19]. Schmidt and Boye [11] employed a phase Doppler anemometer (PDA) for measuring the size and velocity of drops generated by flat and full-cone hydraulic nozzles, operating between 200 and 600 kPa and producing small water impact densities, 0.30-1.7 L/m<sup>2</sup>s. Although, according to the authors, ten different nozzles were characterized, the effect of the nozzle type on the spray characteristics was not described. In experiments performed in the film boiling regime, at temperatures between 300-600  $^\circ\text{C}$  and at constant water impact flux, the heat transfer

coefficient showed a significant increase with the increase in droplet velocity in the range of 3.8 to 6.7 m/s. In contrast, the droplet size had little or no effect on the heat transfer coefficient in the range investigated,  $30 \leq d_{30} \leq 110 \mu\text{m}$ . A study involving internal mixer air-blast atomizers reported volume mean diameters,  $d_{30}$ , and mean velocities,  $u_{av}$ , in the range of 5 to 18  $\mu\text{m}$  and 5 to 31 m/s, respectively, as function of radial position, for  $W=0.0019 \text{ L/s}$  and  $200 \leq p_a, \text{ kPa} \leq 500$  [12]. Also, through measurements with a specially designed device (patternator) it was found that not all the water sprayed reached the collector surface. The amount of wasted water went from 19 to 40 % as the air pressure increased while the heat transfer measurements reported an increase in the boiling heat transfer coefficient with pressure. Although the heat fluxes and heat transfer coefficients during spray cooling have been usually expressed in terms of the water impact flux,  $w$ , the effect of the air pressure, by its concomitant effect on the spray characteristics, has been considered in different forms [3], [13], [14]. These have included the replacement of  $w$  by the kinetic energy [13], or by a set of independent parameters such as volume mean droplet size, volume mean droplet velocity and droplet number density [14] or by the inclusion of the air nozzle pressure,  $p_a$ , in the correlations written in terms of  $w$  [3].

Mathematical-modeling studies have also been carried out to predict the velocity and trajectory of drops in spray and mist jets [15]-[19]. Hatta et al. [15]-[16] developed a two-dimensional (2-D) transient Eulerian-Lagrangian model to describe the motion of air and drops in a nozzle chamber and to calculate their velocities at the nozzle exit. Then, through a perturbation of these non-equilibrium velocities, they simulated the two-phase flow in the free and the impingement regions of the spray. The works considered only particles of 1 and 10  $\mu\text{m}$ , and found that the smaller particles were more susceptible to follow the gas-flow pattern, concentrating in the jet boundary and remaining closer to the solid surface after impingement. Issa and Yao [17] also developed a CFD model to calculate the in-flight motion of droplets and air over a short distance between the nozzle exit and an impingement plane. The authors assumed a distribution of particles with an average size of 40  $\mu\text{m}$ , and simulated their rebounding from the surface considering empirical information on the normal coefficient of restitution as a function of the impinging  $We_{zs}$ . The tangential coefficient of restitution was taken equal to one. The calculations predicted that the larger particles rebounded farther away from the surface, keeping enough of their mo-

mentum to later impinge back on it. Since the calculations assumed that the droplets did not break during impingement, they were intended to simulate conditions with  $We_{zs} < 80$ , this critical value for the break-up of the primary droplets is larger than that indicated in another study [9]. The equation of motion for drops projected horizontally in quiescent air was solved for drops in the range 100 to 1000  $\mu\text{m}$  and velocities of 20 and 50 m/s, finding out that the drops smaller than 100  $\mu\text{m}$  would experience large deflections due to gravity, and would never reach a plane beyond 0.25 m [18].

In a recent study [19] the authors presented a numerical analysis of the fluid flow of air-mist jets, under conditions relevant to secondary cooling of continuously cast thin steel slabs. In the present work, new information on the droplet size and velocity distributions have been obtained through a state of the art PDIA system. As it is seen in the article, the appropriate configuration of the system allowed acquiring statistically meaningful samples of sharp drop images at short focal distances, in sprays and air-mists generated under conditions of practical interest. The drop size distribution measurements allowed improvements on the inputs to the CFD model and the measured velocity distributions permitted a more critical assessment of its validity. Empirical expressions for droplet size distribution were obtained for mists produced by different fan-nozzles operating over a wide range of conditions. The mathematical model is able to predict the drop velocity distribution, water impact density and mist impact pressure, without the use of any adjustable parameters.

## Experimental Work

### *Experimental Setup, Conditions and Procedures*

Figures 1(a) through (c) show the PDIA system, the patternator and the pressure mapping system used for measuring the droplet size and velocity distributions, water impact flux distributions and impact pressure distributions, respectively. Two fan type air-mist nozzles were used in the experiments, a Casterjet 1/2-6.5-90 and a Casterjet 1/2-5-60 (Spraying Systems Co., Chicago, IL). The first nozzle delivers a mist jet with a main expansion semi-angle  $\alpha= 45^\circ$  and typically operates at a setback distance  $z_s= 0.175 \text{ m}$  from the impingement surface. For the second nozzle, these parameters are  $30^\circ$  and  $0.199 \text{ m}$ , respectively. The relationships between the air and water flow rates for different nozzle pressures of these fluids are displayed in the operating diagrams shown in Figs. 2(a)-2(b). From these figures it is seen that there are considerable differences in the operating conditions of the two nozzles.

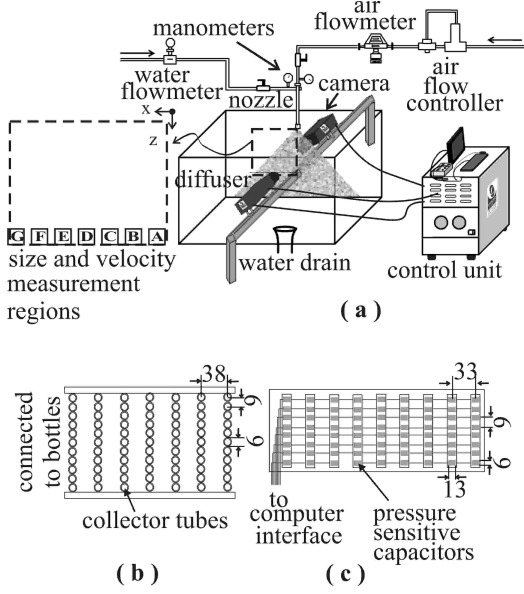


**Figure 1.** Schematics of: (a) PDIA and fluids delivery system, (b) patternator and (c) pressure mapping grid. The lengths are in millimeters.

The triangles drawn in the diagrams indicate the conditions for which measurements were done, and the dashed lines represent the locus of conditions at which the ratio  $A/W=10$ , to the right of these lines the ratio becomes smaller. As seen in Figure 1(a), the supply lines for the fluids were instrumented with valves and digital manometers and flowmeters, which signals were logged in a computer. The air line included an automatic flow controller to minimize variations caused by the compressor. The water flow rates and pressures deviated from the desired value by less than  $\pm 2\%$ . The properties of the fluids and the parameters of the nozzle used are given in Table 1.

#### Drop Size and Velocity Measurement

As it is shown in Figure 1(a) and in the photographs of Figs. 3(a)-3(b) the size,  $d_d$ , and velocity,  $u$ , of individual droplets were determined using a Particle/Drop Image Analyzer system (Oxford Lasers, VisiSizer N60V, Oxford Lasers Ltd., Didcot, United Kingdom). The system acquires and analyzes shadow images of droplets moving through small probe volumes. It employs a dual head Nd:YAG laser that sends light pulses (15mJ at 532 nm) through a fluorescent diffuser that illuminates the region of interest from behind, while shadow images of the subjects are taken with a high resolution (4 Mpixels, 15 Hz) digital camera. The

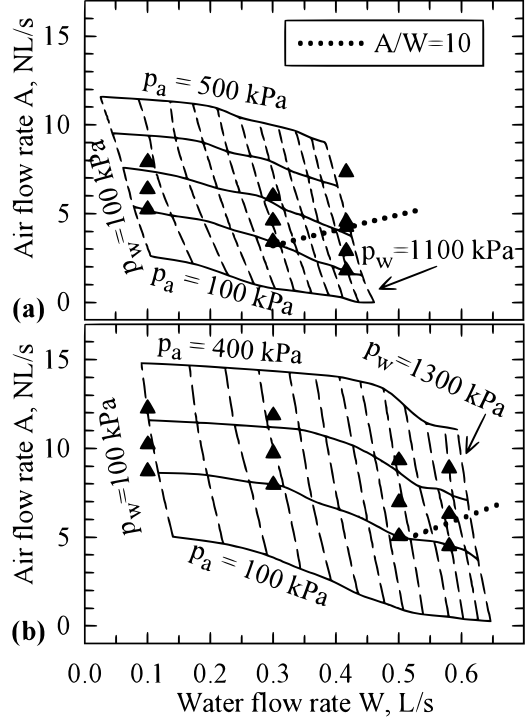


**Figure 2.** Operating diagrams of the air-mist nozzles studied: (a) CJ-1/2-5-60 and (b) CJ-1/2-6.5-90. The triangles indicate the conditions investigated.

Properties of fluids		
$\rho_d; \sigma$	998; $7.28 \times 10^{-2}$	
$\rho; \mu$	1.02; $1.8 \times 10^{-5}$	
Nozzle parameters		
	CJ-1/2-6.5-90	CJ 1/2-5-60
$l_x$	0.01	0.00825
$l_y$	0.00325	0.00235
$l'_x$	0.00585	0.0050
$z_s$	0.175	0.199
$z_{mc}$	0.25	0.020
$\alpha; \theta$	45; 10	30; 9

**Table 1.** Flow conditions, fluid properties and nozzle parameters (these are explained in Figure 4(a)).

particle size range and the velocity limit, for the smallest droplet, that are detected by the system are  $3.5$  to  $5670 \mu\text{m}$  and  $185 \text{ m/s}$  for  $3.5 \mu\text{m}$ , respectively. In this study, the lens configuration was selected to optimize the resolution of drops in the range of  $5$ - $366 \mu\text{m}$ , using field of views of  $2.561 \times 2.561 \text{ mm}^2$  and  $5.245 \times 5.245 \text{ mm}^2$ , with a depth of focus of  $\sim 0.49 \text{ mm}$ . These probe volumes are schematically represented by the regions A-G shown in Fig. 1(a), and

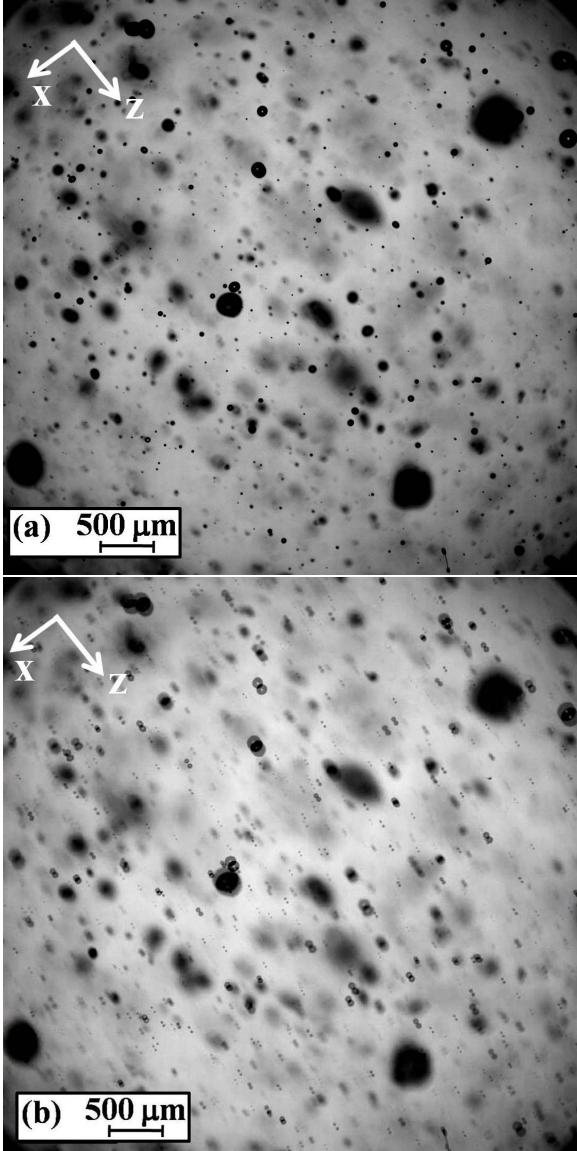


**Figure 3.** Photographs of drops in a probe region: (a) single image, exposure time 4 ns and (b) pair of images in a succession separated by 1.7  $\mu$ s. The nozzle axis direction,  $z$ , appears tilted because of the arrangement designed to minimize water drop deposition on the diffuser and camera, under the very short focal lengths used.

were located over the major symmetry plane of the mist jet at the designated  $z_s$  distance. In double pulse mode, i.e., for simultaneous measurement of size and velocity, the laser and camera were triggered so that consecutive short pulses (lasting 4 ns) separated by a selectable time interval (1.7  $\mu$ s in this study) froze the motion of the subject during each

frame capture; Fig. 3(a) shows a single frame and Fig. 3(b) shows the superposition of two consecutive frames. In the investigation the system was set to analyze in real time 1000 frame-pairs to build-up particle size distribution, velocity distribution, size-velocity correlation and several statistics, e.g.,  $d_{10}$ ,  $d_{30}$ ,  $d_{32}$  and  $u_{av}$ , among others. To enhance the analysis, a series of criteria were defined for background normalization and image thresholding, i.e., to distinguish between the particle shadows and the illuminated background and for restricting the particles analyzed only to those that met certain acceptability criteria. In regard to the determination of size, the criteria for particle consideration had to be based on focal distance, depth of field, background intensity, contact with the borders of the field of view and multiple shadow repetition at the same position. For the determination of velocity, the particle pairs were discriminated by direction, maximum angle deviation and maximum separation, maximum area ratio and maximum halo ratio. The procedures for the definition of the criteria for particle and particle pair consideration are given elsewhere [20]. The number of frames captured provided samples in excess to 5500 drops which is required for obtaining statistical confidence limits of 95 % [21]. The calibration (i.e., the  $\mu$ m/pixel) provided for the camera, lens and magnification used were validated measuring standard circles in a reticule and standard line spacings in a grating, and the agreement was better than 0.5 %.

#### *Water Impact Flux and Air-mist Impact Pressure Measurement*

The local water impact flux,  $w$ , was measured with the patternator shown in Fig. 1(b), orienting the nozzle axis horizontally and pointing to the center of a selected collector cell; each collector was connected to a bottle. The setback distance of the nozzle relative to the patternator corresponded to the nominal  $z_s$  value specified for each nozzle type, as was given previously. While setting the desired water- and air-flow rates during the test the patternator was shielded by a screen, and once the flow stabilized, the screen was removed to initiate the water capture for a sufficiently long time  $t$ . The local water impact flux was calculated as:

$$w = \frac{V}{(A_c \cos\alpha' \cos\theta')t} \quad (1)$$

where  $V$  is the volume of water collected,  $A_c$  is the geometric area of the collector cells and  $\alpha'$  and  $\theta'$  are the angles between the nozzle axis and lines joining the center of the nozzle orifice to the center of the

collectors aligned along the axis perpendicular to the nozzle axis.

The pressure exerted by a mist upon a solid surface was measured using dynamic electronic pressure sensors (Tactilus, Sensor Products LLC, Madison, NJ) arranged in a 9x8 matrix, as shown in Fig 1(c). The matrix of sensors was wrapped with a latex bag and was calibrated by applying known pressures. The mist pressure was sampled at a rate of  $10 \text{ s}^{-1}$  and time averaged values were obtained over a 1 min period.

## Mathematical Model and Computational Scheme

### System Considered and Assumptions

The modeling of air-mists considered the motion, under room temperature conditions, of a two-phase free-jet issuing from a pneumatic nozzle, as it is schematically shown in Figure 4(a). The air phase was treated as continuous in an Eulerian frame of reference and the water droplets were regarded as discreet and randomly dispersed in the continuous phase, and were considered in a Lagrangian frame of observation. Because the visualization of the jets and the measurements of their impact footprints indicated double symmetry over the  $x - z$  and  $y - z$  planes shown in Fig. 4(a), the computational domain included just one quarter of the physical domain. Also, since stable air- and water-flow rates were considered it was assumed that on a time average basis, the flow characteristics of the two-phase jets could be simulated as in steady-state conditions.

In the model, it was assumed that the water stream splattering on the deflector surface was sheared by the air and became atomized, forming drops with the same size distribution as that measured outside the nozzle, i.e., it was assumed that the droplets did not break or coalesce after formation. This statement seems reasonable since drop interaction must be small due to the reduced volume fraction occupied by the drops, even within the mixing chamber of the nozzle ( $<0.08$ ). Also, it was considered that after the drops originated they were transported by aerodynamic drag from the deflector surface to the nozzle exit, i.e., it was assumed that the drops started from a zero axial velocity and reached a certain velocity at the nozzle exit.

### Governing Equations

Under the considerations just described, the governing equations for the air mist flow can be written as,

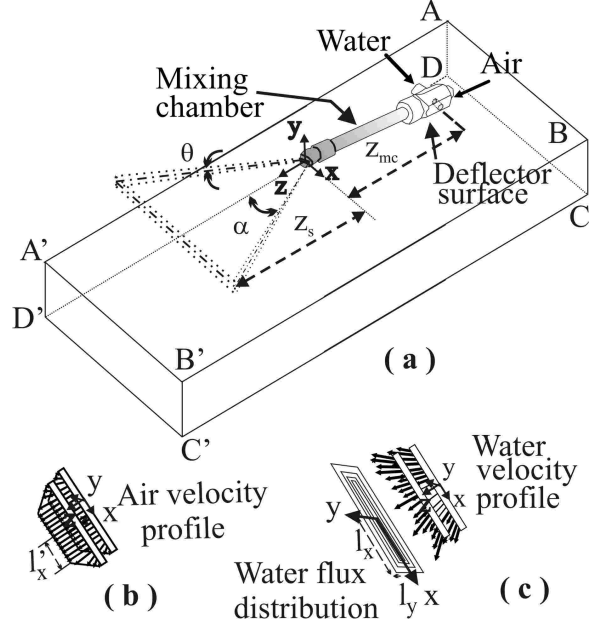


**Figure 4.** Schematics of: (a) system considered and computational domain, (b) air-velocity profiles, and (c) water-velocity profiles and flux distribution assumed at the nozzle orifice.

Continuity equation:

$$\frac{\partial U_i}{\partial x_i} = 0 \quad (2)$$

Navier-Stokes equations:

$$\begin{aligned} \rho U_i \frac{\partial U_j}{\partial x_i} &= -\frac{\partial p}{\partial x_j} \\ &+ \frac{\partial}{\partial x_j} \left[ (\mu + \mu_t) \left( \frac{\partial U_i}{\partial x_j} + \frac{\partial U_j}{\partial x_i} \right) \right] \\ &+ S_i \end{aligned} \quad (3)$$

where  $S_i$  is a source term expressing that the momentum transferred between the air and the drops in a given cell of the fixed Eulerian grid is equal to change in the momentum of all the drops,  $\dot{\eta}$ , passing through the cell over the Lagrangian time step [23], and is given as:

$$S_i = \frac{\pi}{6\rho v_{cell}} \Sigma \dot{\eta} (\rho_d^o u_i^o (d_d^o)^3 - \rho_d^n u_i^n (d_d^n)^3) \quad (4)$$

The turbulence of the air was treated by the  $k - \varepsilon$  model for low Reynolds flows of Lam-Bremhorst modified by Yap [23], and which is given by the following equations:

$$\begin{aligned} \rho U_i \frac{\partial k}{\partial x_i} &= \frac{\partial}{\partial x_i} \left[ \left( \mu + \frac{\mu_t}{\sigma_k} \right) \frac{\partial k}{\partial x_i} \right] \\ &+ \mu_t \left( \frac{\partial U_i}{\partial x_j} + \frac{\partial U_j}{\partial x_i} \right) \frac{\partial U_i}{\partial x_j} \\ &- \rho \varepsilon \end{aligned} \quad (5)$$

$$\begin{aligned} \rho U_i \frac{\partial \varepsilon}{\partial x_i} &= \frac{\partial}{\partial x_i} \left[ \left( \mu + \frac{\mu_t}{\sigma_\varepsilon} \right) \frac{\partial \varepsilon}{\partial x_i} \right] \\ &+ f_1 c_1 \mu_t \frac{\varepsilon}{k} \left( \frac{\partial U_i}{\partial x_j} + \frac{\partial U_j}{\partial x_i} \right) \frac{\partial U_i}{\partial x_j} \\ &- \rho f_2 c_2 \frac{\varepsilon^2}{k} \end{aligned} \quad (6)$$

where the turbulent dynamic viscosity is defined as follows:

$$\mu_t = \rho f_\mu C_d \frac{k^2}{\varepsilon} \quad (7)$$

The values of the constants  $\sigma_k$ ,  $\sigma_\varepsilon$ ,  $c_1$ ,  $c_2$  and  $C_d$  and the expressions for the functions  $f_1$  and  $f_2$  appearing in (5)-(7) are listed in Table 2.

The equation of motion for individual drops accounted for the effects of the aerodynamic drag and gravity, and thus it was expressed as follows:

$$\begin{aligned} \frac{du_i}{dt} &= \frac{3}{4} C_D \frac{\rho}{\rho_d d_d} |U_i - u_i| (U_i - u_i) \\ &+ \left( 1 - \frac{\rho}{\rho_d} \right) g_i \end{aligned} \quad (8)$$

The drag coefficient  $C_D$  was assumed to vary with the particle Reynolds number,  $Re_d$ , according to the expressions given in Table 2. The trajectory of the drops was computed from the change with time of the components of the position-vectors, as follows:

$$\frac{dx_i}{dt} = u_i \quad (9)$$

#### Boundary and Initial Conditions

In the case of a free, non-impinging air-mist jet, the turbulent equations of motion for the air phase, (2), (3), (5) and (6), were solved by applying the following conditions at the boundaries displayed in Figure 4(a):

- Ambient conditions at the boundaries ABCD, A'B'C'D', ABB'A' and BCC'B', specified as follows:

$$P = P_{amb} ; k = \varepsilon = 0 \quad (10)$$

To approach these conditions, the computational boundaries were located far away from the jet, as it is schematically illustrated in the figure.

- Symmetry conditions at the boundaries ADD'A', DCC'D', given as:

$$U_j = \frac{\partial U_i}{\partial x_j} = \frac{\partial k}{\partial x_j} = \frac{\partial \varepsilon}{\partial x_j} = 0 \quad (11)$$

where  $j$  represents the index for the coordinate normal to the respective symmetry plane.

To examine a free jet impinging on a solid surface located at  $z = z_s$ , the boundary A'B'C'D' was placed at this position, and non-penetration and non-slip conditions were specified as follows:

$$U_i = k = \varepsilon = 0 \quad (12)$$

Similar conditions were specified at the external wall of the nozzle.

The nozzle orifice corresponded to an internal boundary where air velocity profiles such as those shown in Figure 4(b) were prescribed. Along the  $x$ -direction, the velocity profile was uniform over the flat hollow portion of the flanged orifice having a length  $l'_x$ , as indicated in Fig. 4(b), in the rest of the orifice they decreased to zero varying in angle from 0 deg to  $\alpha$  deg at the edge; this distribution was held constant throughout the whole thickness direction of the orifice. The velocity profile was suggested by the geometry of the flanged orifice and is supported by the results presented in a later section. The mathematical expressions for the air velocity profiles at the orifice are given in Table 2, together with the expressions used to evaluate  $k$  and  $\varepsilon$  at this boundary.

To assign initial conditions for droplet motion to be used in (8) and (9), a first step was to design a way to distribute drops of different size over the nozzle orifice. To do this, the nozzle orifice was simulated as a grid of ports,  $k$ , releasing drops with the volume,  $\nu_d (= 1/6\pi d_d^3)$ , and frequency,  $\eta_{d,k}$ , needed to satisfy the water-flow rate,  $W$ , as follows:

$$W = \sum_{k=1}^{n_{p,t}} \eta_{d,k} \nu_{d,k} \quad (13)$$

Furthermore, this water flow was assumed to be distributed according to an obelisk-shaped distribution [3] as that shown in Figure 4(c). Since the PDIA technique resolved drops over the whole size range, the number of ports assigned to each drop size category  $d_d$  was prescribed according to the volume frequency histogram, corresponding to the particular nozzle and operating conditions considered. The drop size assigned to each port was

Constants and functions involved in the turbulence model	
$C_1=1.44$ ; $C_2=1.92$ ; $C_d=0.09$ ; $\sigma_k=1.0$ ; $\sigma_\varepsilon=1.3$ $f_\mu=(1-\exp(-0.0165\text{Re}_{z'}))^2 \left( 1 + \frac{20.5}{\text{Re}_t} \right)$ ; $f_1=1 + \left( \frac{0.05}{f_\mu} \right)^3$ ; $f_2=1 - \exp(-\text{Re}_t^2)$	
where	$\text{Re}_{z'} = \frac{\sqrt{kz'}}{\nu}$ ; $\text{Re}_t = \frac{k^2}{\nu\varepsilon}$
Drag coefficient expressions	
Stokes law region, $\text{Re}_d < 2$	$C_D = 24/\text{Re}_d$
Intermediate region, $2 \leq \text{Re}_d \leq 500$	$C_D = 10/\sqrt{\text{Re}_d}$
Newton's law region, $500 \leq \text{Re}_d \leq 2 \times 10^5$	$C_D = 0.44$
where	$\text{Re}_d = \frac{d_d  U_i - u_i }{\nu}$
Boundary conditions at the nozzle exit	
Air	Water
$0 \leq x \leq l'_x$ $u_{x,o} = 0, u_{y,o} = 0, u_{z,o} = u_{z,max}$	$u_{x,o} = u_{z,t} \sin(\alpha x/l_x)$
$l'_x \leq x \leq l_x$ $u_{x,o} = u_{z,o} \tan\alpha_x, u_{y,o} = 0$	$u_{y,o} = u_{z,t} \sin(\theta y/l_y)$
$u_{z,o} = u_{z,max}(l_x - x)/(l_x - l'_x)$	$u_{z,o} = [u_{z,t}^2 - u_{x,o}^2 - u_{y,o}^2]^{1/2}$
$\alpha_x = \alpha(x - l'_x)/(l_x - l'_x)$	
$u_{z,max} = (A^* + W)/[2l_y(l_x + l'_x)]$	
$0 \leq x \leq l_x$ $k_o = 0.01u_{z,max}^2$ ; $\varepsilon_o = 2k_o^{1.5}(l_x + l_y)/(4l_x l_y)$	

\*A is computed at the local conditions, 25 °C and 86 kPa.

**Table 2.** Auxiliary equations.

chosen stochastically through a random number generator.

The initial conditions then used in (8) and (9) were assigned to each port of the nozzle orifice, such that at  $t = 0$ :

$$u = u_o \quad \text{and} \quad x = x_o \quad (14)$$

As mentioned in the beginning of the section, the initial velocity,  $u_o$ , of the drops was prescribed according to the velocity reached by the drops when accelerated by the air stream from rest, from the deflection plate to the nozzle exit. For all the drop sizes considered, the numerical solution of the equation of motion, using Euler's method, predicted that the drops reached their terminal velocity before reaching the nozzle orifice, thus  $u_{z,o} = u_{z,t}$ . The variation of the terminal velocity with particle size is given in Fig. 5 for a particular set of conditions. As suggested by the observed drop trajectories [19], according to the position assigned to the drop the angle of the velocity varied from 0 deg to  $\alpha$  deg in the  $x$ -direction and from 0 deg to  $\theta$  deg in the  $y$ -direction. A schematic representation of the velocity vectors of the drops is displayed in Fig. 4(c)

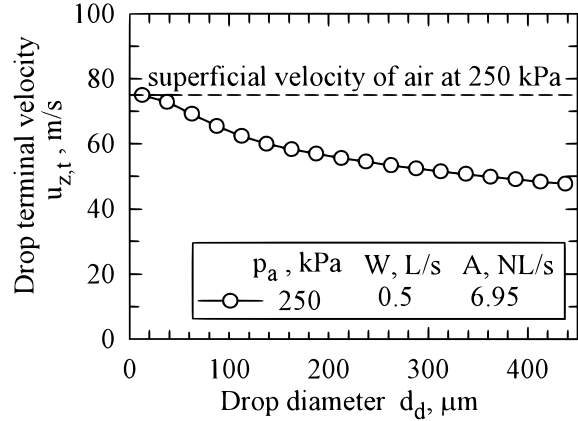


**Figure 5.** Terminal drop velocities as a function of size calculated for superficial air velocities based on the effective cross sectional area of the orifice of a CJ-1/2-6.5-90 nozzle and the given conditions.

and the expressions for the  $u_{x,o}$  and  $u_{y,o}$  velocity components are given in Table 2.

### Solution Procedure

The Eulerian and Lagrangian equations of the model were solved using the control volume method and the particle tracking facility implemented in Phoenix. The meshes used had 130x25x105 and 128x25x99 control volumes for the impacting and non-impacting problems and the number of ports was 12x100. The convergence criterion specified a total residual for all the dependent variables  $\leq 10^{-3}$ .

## Results and Discussions

### Droplet Size and Velocity Characterization

The PDIA technique used in this work is a multiple droplet counting technique that samples the drops occupying instantaneously a given volume, as it is shown in Figs. 3(a)-3(b), and in that sense is a spatial technique. However, since the size and velocity of the drops present in the volume are determined simultaneously, liquid flux distributions can also be estimated.

As indicated in the measurement subsection, the size and velocity measurements were done at regions A through G shown in Figure 1(a). Figure 6(a) through 6(c) show the results of number frequency and volume frequency of droplet size, together with the cumulative distributions and the velocity histogram obtained over all the probe volumes A-G, for a Casterjet 1/2-6.5-90 nozzle operating under the given conditions. Comparing in Figs. 6(a) and 6(b), the frequency and cumulative histograms for the number and volume of the drops corresponding to the measured sizes, it is evident that the smaller size droplets ( $\leq 50 \mu\text{m}$ ) constitute a very large proportion, 96.9 %, of the total number of drops. However, these drops account for a relatively small proportion of the total volume (25.6 %). The volume histograms such as that shown in Fig. 6(a) revealed relatively isolated droplets with large sizes contributing a significant amount of volume to the sample. These events illustrated the need to carefully ensure that adequate samples were obtained. By increasing the number of frames taken, the likelihood of observing these infrequent droplets increased. ASTM guidelines [24] state that the largest drop size reported should make up less than 1 % of the volume of the spray flux, as reported in Figs. 6(a)-6(b).

The distribution of the magnitude of the velocity for regions A through G is displayed in Fig. 6(c), where it is seen that the velocities span a wide range. The number frequency distributions of the measured droplet velocities resemble closely normal distributions. The correlation between the magnitude of the velocity and the droplet diameter, shown in Fig. 7, indicated that the smaller droplets had velocities

that varied over a wider range than the larger ones, possibly because of the larger effect that the air flow has on them.

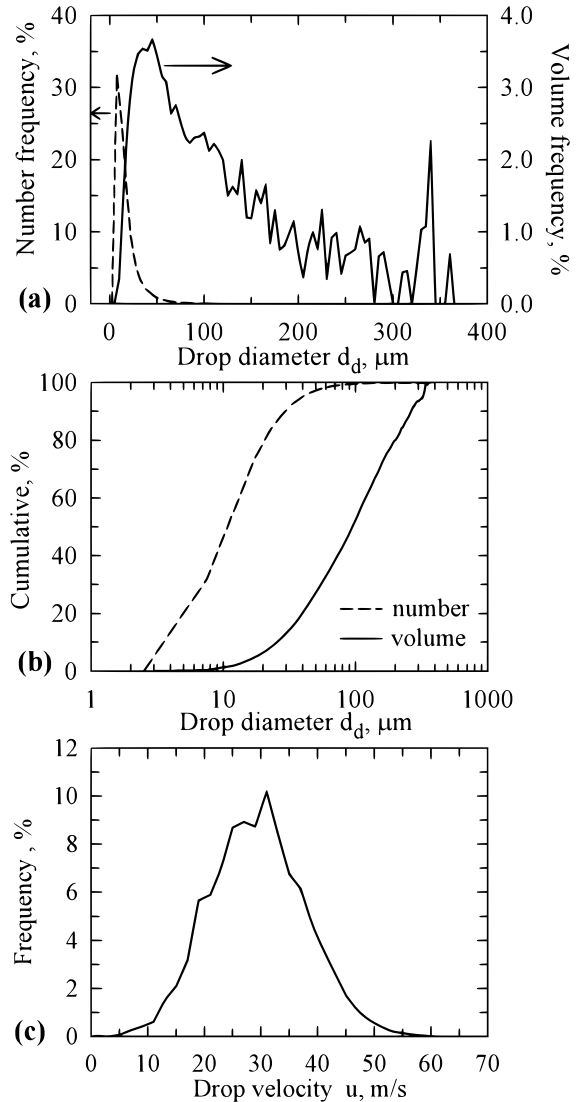


**Figure 6.** Measured: (a) number and volume frequency distributions of the diameter of droplets, (b) cumulative number and volume distributions of droplet diameters and (c) number frequency distribution of the velocity of drops. The results lump the measurements in all probe regions A-G, obtained with a CJ-1/2-6.5-90 nozzle operating at  $W = 0.5\text{L/s}$  and  $p_a = 320\text{ kPa}$ .

### Characterization of Droplet Size Distribution

The experimental data for a Casterjet 1/2-6.5-90 nozzle operating under the conditions corresponding to the triangles drawn in Fig. 2(b) were analyzed

to determine the droplet size distribution functions representing best the number and volume spectra of the diameter data. Various functions were tested by comparing statistical parameters estimated from the correlations, for the conditions shown in Fig. 2(a), with the corresponding parameters calculated from the distributions measured for a Casterjet 1/2-5-60 nozzle.

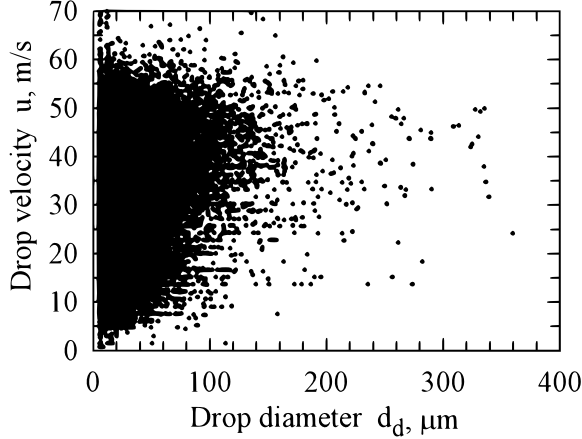


**Figure 7.** Measured correlation between drop velocity and diameter obtained over the probe regions A-G, with a CJ-1/2-6.5-90 nozzle operating at  $W = 0.5L/s$  and  $p_a = 320$  kPa.

The experimental data was fitted to the functions commonly applied [25]-[26] for the characterization of the droplet size distribution in liquid sprays, namely: Log-Normal (LN), Rosin-Rammler (RR), Modified Rosin-Rammler (MRR), Nukiyama-Tanasawa (NT) and Upper-Limit (UL) distributions. All these functions with the exception of the upper limit have the advantage of including only two parameters: a representative size parameter, and a dispersion parameter. The UL distribution uses additionally the maximum droplet size as a parameter. Figures 8(a) and 8(b) compare the experimental number size and volume size distributions, respectively, with the calculated distribution functions for the particular set of conditions given with the figures. From them it is appreciated that the LN function gives the best fitting for the measured number distribution and that the NT function does this for the volume frequency distribution. Figure 8(c) resumes the error differences between the calculated and experimental cumulative number and cumulative volume frequencies, obtained under the different conditions studied. From the figures it is seen that the error is low, below 10 %. The equations for the LN and NT function distributions are given as:

$$\frac{dN}{dd_d} = \frac{1}{d_d \ln \sigma_g \sqrt{2\pi}} \exp \left[ \frac{-1}{2(\ln \sigma_g)^2} \left( \ln \left( \frac{d_d}{d_{d,ng}} \right) \right)^2 \right] \quad (15)$$

$$\frac{dV}{dd_d} = \frac{a^{6/\delta}}{\Gamma(6/\delta)} d_d^5 \exp(-ad_d^\delta) \quad (16)$$

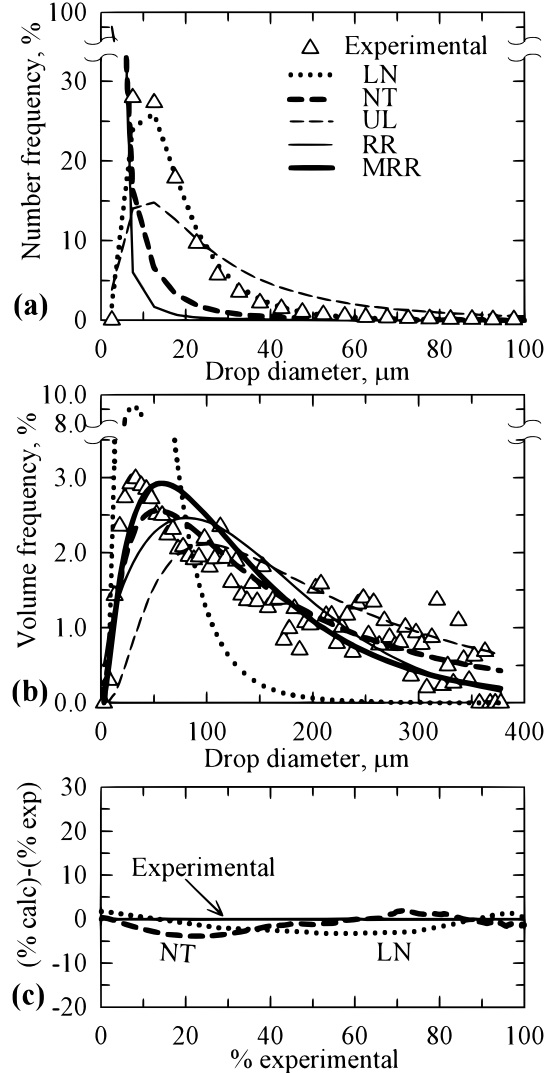


**Figure 8.** Comparison between measured and fitted: (a)-(b) number and volume frequency distributions of droplet diameter, respectively, for a CJ-1/2-6.5-90 nozzle operating at  $W = 0.58$  L/s and  $p_a = 279$  kPa. (c) Error differences between fitted and calculated cumulative number and cumulative volume frequencies for all the conditions studied appearing in Figure 2(b).

The size parameters,  $d_{d,ng}$  and  $a$ , and the dispersion parameters,  $\sigma_g$  and  $\delta$ , appearing in distributions functions (15) and (16) were correlated to the water- and air-nozzle pressures,  $p_w$  and  $p_a$ , according to the following equation:

$$y = a_o + bp_w + cp_a + dp_w^2 + ep_a^2 + fp_wp_a + gp_w^3 + hp_a^3 + ip_wp_a^2 + jp_w^2p_a \quad (17)$$

The values of the coefficients are given in Table 3, together with the correlation coefficients of the equations, which it is seen to be  $\geq 0.98$ . Equations (15) through (17) were used to evaluate the diameters  $d_{10}$ ,  $d_{20}$ ,  $d_{30}$  and  $d_{32}$  for a Casterjet 1/2-5-60 nozzle, operated under the conditions marked by the triangles in Figure 2(a). The comparison between the measured and estimated values of these statistical quantities is shown in Table 4, in terms of percentage differences. It is seen that in general the percentage differences between measured and calculated diameters are smaller than 30 %. This agreement seems quite reasonable since the characteristic diameters  $d_{30}$  and  $d_{32}$  are strongly influenced by the droplet diameter, particularly of the larger drops.

#### *Influence of Air-nozzle Pressure on Droplet Size and Velocity*

Figures 9(a) and 9(b) show the number frequency distributions of droplet sizes and droplet velocities for three air nozzle pressures, the histograms group together the data for regions A through G. From Figure 9(a) it is seen that as the air pressure increases, the relative fraction of the smaller size range of droplets in the mist increases at the expense of larger size ranges. However, the maximum droplet diameters remain unaltered by the increase in pressure, within the range studied. The geometric standard deviations,  $\sigma_g$ , of L-N drop size distributions at  $p_a$  of 205, 279 and 340 kPa were 1.91, 1.82, 1.81, respectively, this shows that increasing the air pressure does not modify appreciably the width of the size distribution. In contrast to the distribution of droplet size the distributions of droplet velocities shown in Fig. 9(b) display considerable displacements of the distributions towards larger velocities as  $p_a$  increases, within the range considered. In the case of the distributions of droplet velocities, it is noteworthy that, the fraction of the smaller droplet velocities decrease considerably and large velocities become more frequent as the air pressure increases. The standard deviations of the droplet velocities at  $p_a$  of 205, 279 and 340 kPa were 5.1, 6.9 and 8.7,

Log-Normal		
	$y = \sigma_g$	$y = d_{d,ng}$
$a_o$	3.391x10 <sup>0</sup>	4.155x10 <sup>0</sup>
$b$	5.414x10 <sup>-4</sup>	-1.100x10 <sup>-3</sup>
$c$	-1.772x10 <sup>-2</sup>	1.747x10 <sup>-1</sup>
$d$	2.391x10 <sup>-7</sup>	6.303x10 <sup>-6</sup>
$e$	6.793x10 <sup>-5</sup>	-7.194x10 <sup>-4</sup>
$f$	-4.612x10 <sup>-6</sup>	-1.984x10 <sup>-5</sup>
$g$	4.675x10 <sup>-11</sup>	-1.010x10 <sup>-9</sup>
$h$	-8.912x10 <sup>-8</sup>	8.908x10 <sup>-7</sup>
$i$	1.314x10 <sup>-8</sup>	3.936x10 <sup>-8</sup>
$j$	-1.811x10 <sup>-9</sup>	-1.167x10 <sup>-8</sup>
$r^2$	0.99	1.00
Nukiyama-Tanasawa		
	$y = a$	$y = \delta$
$a_o$	-1.319x10 <sup>2</sup>	3.244 x10 <sup>0</sup>
$b$	6.747x10 <sup>-3</sup>	6.506 x10 <sup>-4</sup>
$c$	1.641x10 <sup>0</sup>	-3.641 x10 <sup>-2</sup>
$d$	5.398x10 <sup>-5</sup>	-4.775 x10 <sup>-7</sup>
$e$	-6.260x10 <sup>-3</sup>	1.444 x10 <sup>-4</sup>
$f$	-1.349x10 <sup>-4</sup>	-3.635 x10 <sup>-6</sup>
$g$	-2.067x10 <sup>-8</sup>	6.783 x10 <sup>-11</sup>
$h$	7.704x10 <sup>-6</sup>	-1.846 x10 <sup>-7</sup>
$i$	5.560x10 <sup>-7</sup>	1.805 x10 <sup>-9</sup>
$j$	-7.494x10 <sup>-8</sup>	1.702 x10 <sup>-9</sup>
$r^2$	0.98	0.98

**Table 3.** Values of the coefficients appearing in Equation (17).

$p_w$ , kPa	$p_a$ , kPa	$\%_e d_{10}$	$\%_e d_{20}$	$\%_e d_{30}$	$\%_e d_{32}$
150	205	1.7	-0.4	20.0	66.2
165	257	6.1	3.6	22.8	33.9
185	320	8.2	6.2	47.7	20.2
575	205	5.6	0.8	12.9	-25.3
615	257	3.1	-1.0	20.1	31.6
655	320	4.2	0.6	35.9	36.2
985	205	-5.4	-14.3	-11.1	-44.9
1015	257	-4.4	-12.7	-0.9	53.5
1060	320	-0.4	-6.7	13.4	-3.3

**Table 4.** Percentage errors between fitted and measured statistical parameters of droplet diameter, for mists produced by a CJ-1/2-5-60 nozzle operating under different water- and air-nozzle pressures.

respectively, indicating that the velocity spectrum broadens as the pressure increases.

Figure 10(a) shows the numerical mean diameter,  $d_{10}$ , the volume mean diameter,  $d_{30}$ , and the Sauter mean diameter,  $d_{32}$  obtained at air nozzle

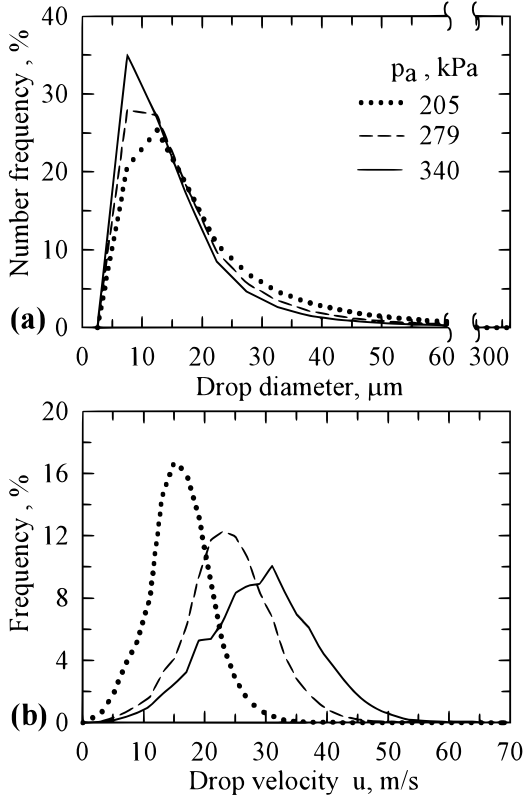


**Figure 9.** Comparisons of measured number frequency distributions of: (a) droplet diameters and (b) drop velocities at different air-nozzle pressures. The distributions lump the data obtained for regions A-G with a CJ-1/2-6.5-90 nozzle operating at  $W = 0.58$  L/s.

pressures of 205, 279 and 340 kPa. The three size parameters decrease with the increase in pressure, particularly the Sauter mean diameter, which represents the size of a droplet that has the same ratio of surface area to volume as that of the entire spray. Figure 10(b) presents the variation of the arithmetic mean velocity,  $u_{av}$ , and the volume weighted mean velocity,  $u_v$ , with pressure, in the range investigated. From the figure, it is seen how rapidly the values of these quantities increase with the air nozzle pressure. The velocity  $u_v$  stands for the velocity that the total volume of liquid should have to own the total momentum of the droplets in the entire spray, passing through the measuring plane.

The variation of the Sauter mean diameter with position is shown in Fig. 11 for different air pressures. The results indicate that the finer drops tend to be located in the inner region of the mist jet and that the larger ones move around the periphery. The

rotational motion of the drops while traveling in the mixing chamber must tend to segregate the largest drops to the periphery and hence they should exit close to the edges of the orifice. In agreement with

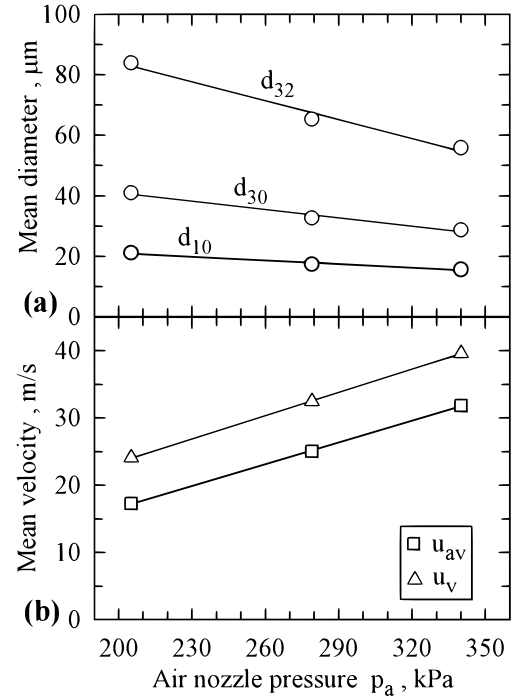


**Figure 10.** Measured: (a) mean diameters variation and (b) mean velocities variations with air-nozzle pressure. The data from all probe regions A-G were used for the averages and correspond to a CJ-1/2-6.5-90 nozzle operating at  $W = 0.58$  L/s.

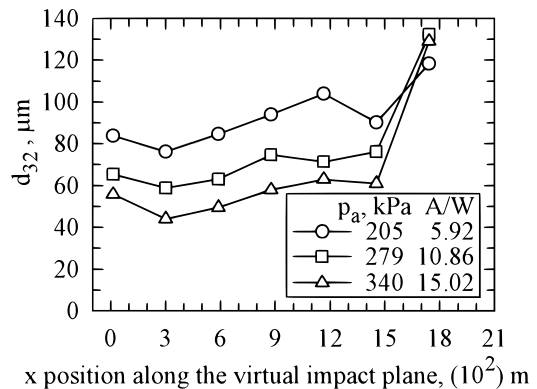
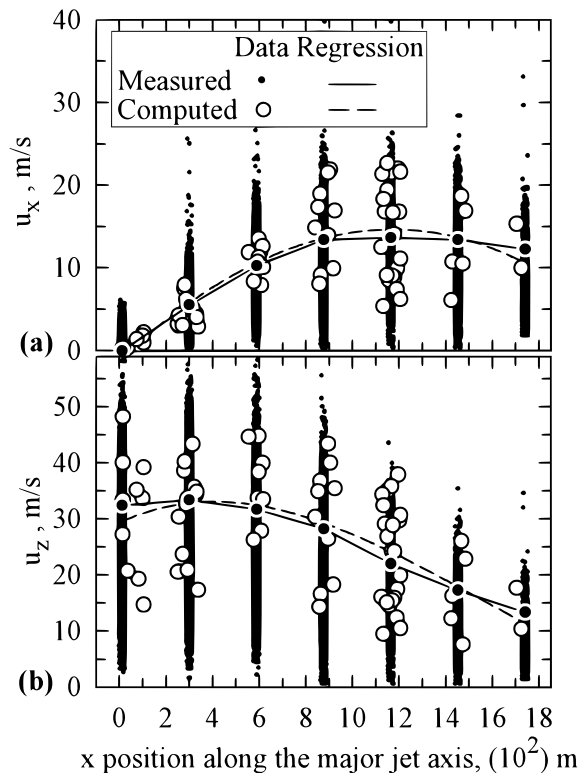


**Figure 11.** Measured variation of Sauter mean diameter with position, for different nozzle operating conditions. The data correspond to a CJ-1/2-6.5-90 nozzle operating at  $W = 0.58$  L/s.

the droplet size distribution the figure shows that as the air pressure increases, the profile of Sauter mean diameters display smaller values. However, the diameters of the larger droplets at the periphery of the jet seem to be a little affected by the pressure.

### Computational Results

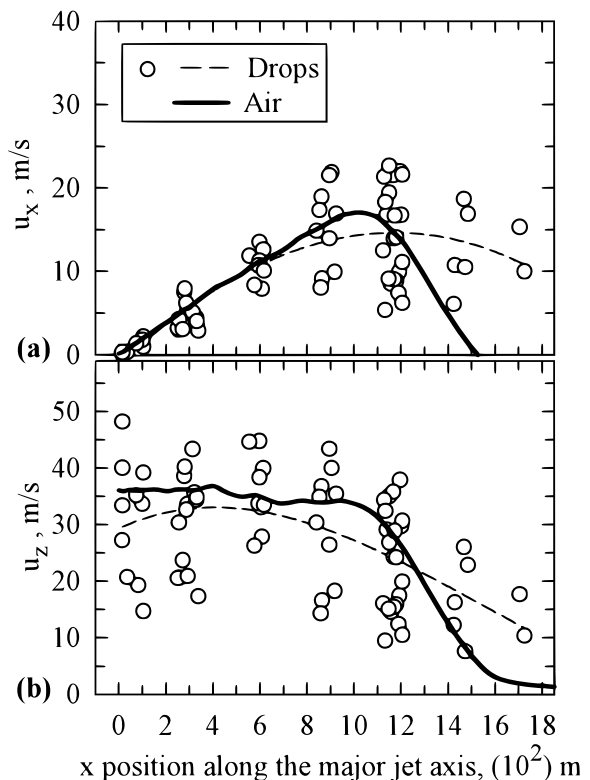
The computed and measured  $x$ - and  $z$ -velocity components of drops moving through the probe volumes, A through G, located at a distance  $z_s=0.175$  m from the orifice of a Casterjet 1/2-6.5-90 nozzle are shown in Fig. 12, for a particular set of operating conditions. The agreement of the computational results with the measurements is quite good. The dispersion of both types of results arises from the randomness with which drops of different size may leave from diverse orifice sites and from the distinctive interaction that the drops would have with air, depending on their size and relative velocity. As indicated by the lines in the figure, the average dro-



**Figure 12.** Comparison between experimental and computed: (a)  $x$ -velocity components and (b)  $z$ -velocity components of drops, as a function of the  $x$ -position. The results correspond to a CJ-1/2-6.5-90 nozzle operating at  $W = 0.58$  L/s and  $p_a = 279$  kPa.

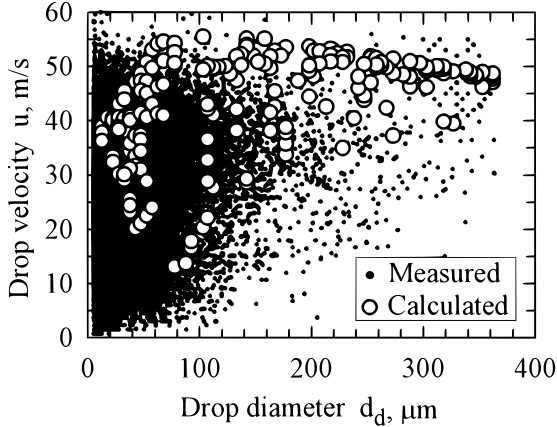
plet velocities obtained from the experimental and computational data are very similar, despite that the computational sample considers that all particles emerge only from 1200 ports and thus results only in this number of trajectories. This suggests that the model accounts for the main features of the actual system.

Figure 13 shows the profiles of the  $z$ -velocity components of the air and droplet phases, computed across the major-symmetry plane of the jet for a distance  $z_s=0.175$  m. The figure indicates that inside the core of the air-mist jets, the continuous and discrete phases move at similar velocities, so that their relative velocity is small, and thus, in general the drops can maintain a relatively high velocity up to the plane located at  $z_s=0.175$  m. In the periphery of the jet, the velocity of the air-phase falls rapidly and the drops follow this tendency, although as expected due to their inertia, their velocity declines more slowly. The correlation between droplet velocity and droplet size is presented in Figure 14. The



**Figure 13.** Computed profiles of the air and drop velocity components in the (a)  $x$ - and (b)  $z$ -directions. The results correspond to a CJ-1/2-6.5-90 nozzle operating at  $W = 0.58$  L/s and  $p_a = 279$  kPa.

experimental measurements, presented in the figure, show that drops with the same size exhibit a wide range of velocities and this behavior is also reflected by the model results. In the model, droplets with a single size left the nozzle from different sites but with a prescribed single velocity, hence, the variation in droplet velocity for a single droplet size arises mainly from the interaction that the droplets have with the local motion of the air-phase during their flight.



**Figure 14.** Comparison between computed and measured drop velocity-droplet diameter correlations. The results lump the data of regions A-G and correspond to a CJ-1/2-6.5-90 nozzle operating at  $W = 0.58$  L/s and  $p_a = 279$  kPa.

The flux of impacting water, which is an important overall property of sprays in spray cooling was evaluated from the parameters associated with the collective trajectories of droplets impinging on small area elements,  $A(x, y)$ , of the impact plane, according to the following expression:

$$w = \frac{1}{A(x, y)} \sum_{k=1}^n \eta_{d,k} \nu_{d,k} \quad (18)$$

where  $k$ ,  $\eta_{d,k}$  and  $\nu_{d,k}$  represent trajectories, number flow rate and volume of individual droplets. An example of the computed and measured water impact flux maps is reported in Fig. 15, for a specific set of conditions. The agreement between both sets of results is excellent. Comparing the assumed water flux distribution at the nozzle orifice, shown in Fig. 4(c), with the water flow footprint at  $z = z_s$  is apparent that the typical dog-bone-shape displayed by the last one must arise from the interaction of the droplets with the air, that deviate the drops from straight trajectories. As seen in the Figure 15

the water impact fluxes of interest to continuous casting are much higher than those that have been typically studied before in connection with spray cooling [11], [12], [17].

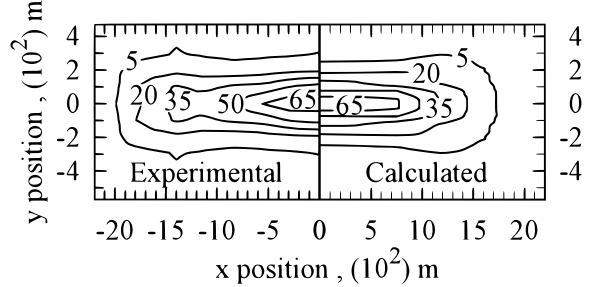


**Figure 15.** Measured and computed water impact flux contours for a CJ-1/2-6.5-90 nozzle operating at  $W = 0.5$  L/s and  $p_a = 257$  kPa.

Similarly to  $w$ , the droplet number flux,  $\dot{N}$ , is calculated based on the properties of the trajectories of droplets falling upon area elements  $A(x, y)$ , the water flow rate,  $Q_k$ , and droplet diameter,  $d_{d,k}$ , according to the following expression:

$$\dot{N} = \frac{1}{A(x, y)} \sum_{k=1}^n \frac{Q_k}{1/6(d_{d,k})^3} \quad (19)$$

A contour plot of the droplet number flux for a specific set of conditions is shown in Fig. 16, the values appearing in the contours correspond to the logarithm of the quantity. According to these model results the water number flux varies from the center to the edges of the footprint from  $10^4$  drops/mm<sup>2</sup>ms to 1 drop/mm<sup>2</sup>ms.

For a more extensive validation of the CFD model, the measured impact-pressure fields, obtained with the pressure mapping system, can be compared with values calculated according to the following formula, which again involves quantities related to the characteristics of the droplet trajectories in the mist:

$$p_{zs}(x, y) = \frac{\rho}{2A(x, y)} \sum_{k=1}^n \dot{\eta}_{d,k} \nu_{d,k} u_{zs,k} + P_{A(x,y)} \quad (20)$$

where  $u_{zs,k}$  is the velocity of individual drops reaching the impact plane at  $z = z_s$  while moving along a trajectory  $k$  and  $P_{A(x,y)}$  is the pressure applied by the air-phase on the surface element centered around a node with coordinates  $x - y$ . The experimental and computed pressure maps are shown in Fig. 17,

where it can be seen that the agreement between both maps is again quite good.

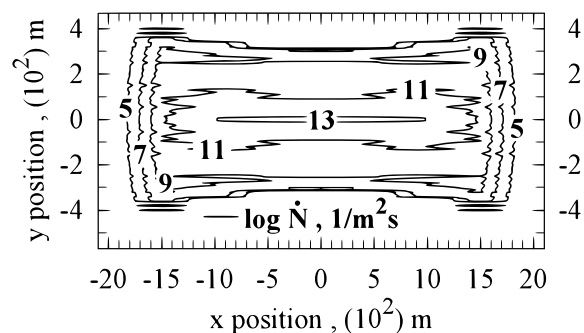


**Figure 16.** Computed droplet number flux contours for a CJ-1/2-6.5-90 nozzle operating at  $W = 0.5$  L/s and  $p_a = 257$  kPa.

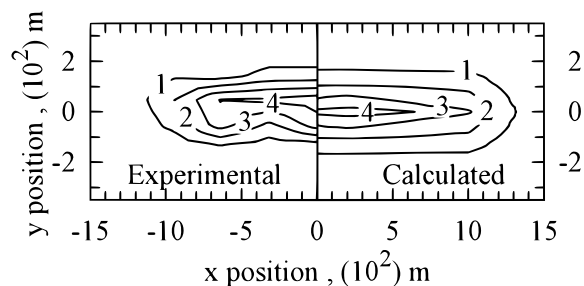


**Figure 17.** Measured and computed mist impact pressure contours for a CJ-1/2-6.5-90 nozzle operating at  $W = 0.5$  L/s and  $p_a = 320$  kPa.

## Summary and Conclusions

A comprehensive experimental study, involving measurements of droplet size, droplet velocity, droplet trajectory, velocity-size correlation, water impact flux and water impact pressure, was carried on air-mist jets generated under conditions of interest in the secondary cooling system of continuous casting machines for the production of thin steel slabs. The droplet size measurements allowed characterizing the number and volume distributions found in air-mist fan nozzles and thus provided the vital information needed to simulate the dynamics of air-mist jets. An Eulerian-Lagrangian model coupling the turbulent Navier-Stokes equations and the equation of motion for the discrete-phase - consisting of multi-size drops, exiting a nozzle at different velocities from stochastically chosen positions - was developed. The CFD model rendered very good estimates of the dynamics of fan air-mists.

The direct information obtained about the effect of air-nozzle pressure on droplet size and droplet velocity is helping us to elucidate the causes behind the observed intensification of spray cooling under these conditions, and finally optimize the operation of secondary cooling systems. This work is part of a research program on the behavior of air-mists employed in continuous casting, which involves studies at low and high temperature conditions.

## Acknowledgments

The CINVESTAV authors are grateful to the National Council of Science and Technology of Mexico (CONACYT) for financial support through grant No. 57836. JIMM wish to thank CONACYT for his scholarship grant. The authors want to express their sincere gratitude to Prof. Ernesto Gutiérrez of RPI at Hartford, for his critical review of the manuscript.

## Nomenclature

$a$	Size parameter from Nukiyama-Tanasawa distribution, Eq. (16)
$a_o, b, c, d, e$	Coefficients of the regression function given by Eq. (17).
$f, g, h, i, j$	
$A$	air flow rate at normal conditions ( <i>i.e.</i> , 0 °C, 101.3 kPa) (NL/s), or ambient conditions (25 °C, 86 kPa), L/s
$A(x, y)$	local area in impact plane centered around coordinates, $x, y$
$A_c$	cross section area of collector cells in patternator, m <sup>2</sup>
$c_1, c_2, C_d$	constants in the turbulence model
$C_D$	drag coefficient
$d_d$	drop diameter, m
$d_{d,ng}$	Size parameter in Log-Normal distribution, Eq. (15)
$d_{pq}$	diameter moments, $= (\sum_{i=1}^n d_i^p / \sum_{i=1}^n d_i^q)^{1/(p-q)}$ (p,q)=(1,0),(2,0),(3,0),(2,3), m
$\%_e d_{pq}$	Error difference of diameter moments $= (d_{pq,exp} - d_{pq,comp}) / d_{pq,exp} \times 100$
$f_\mu, f_1, f_2$	functions in turbulence model
$g$	acceleration due to gravity, m/s <sup>2</sup>
$k$	turbulence kinetic energy, m <sup>2</sup> /s <sup>2</sup>

$l_x, l_y, l'_x$	half length and half width nozzle orifice and half length of hollow portion of nozzle orifice, respectively, m	$z_o, z_{mc}, z_s, z'$	initial position of drops in mixing chamber; length of mixing chamber; setback distance; distance from solid surface, m
$n$	number of drops trajectories, in the model, that impinge upon area $A(x, y)$ , Eqs.(18)-(20); or total number of drops used for determining the diameter moments	Greek symbols	
$n_p$	port number or number of ports	$\alpha, \theta$	jet expansion half angles in x and y directions, deg
$N, \dot{N}$	number frequency of drops with diameter $d_d$ ; droplet number flux, drops/m <sup>2</sup> s	$\alpha', \theta'$	angles between the nozzle axis and lines joining the center of the nozzle orifice to the center of the collectors aligned along the axis perpendicular to the nozzle axis.
$p_a, p_w$	air- and water-nozzle pressures, kPa	$\delta$	dispersion parameter from Nukiyama-Tanasawa distribution, Eq. (16).
$p_{zs}$	pressure applied by a mist impinging on a surface, kPa	$\varepsilon$	dissipation rate of turbulence kinetic energy, m <sup>2</sup> s <sup>-3</sup>
$P_A, P$	local pressure applied by the air in a mist jet impinging on a surface; pressure, kPa.	$\Gamma(z)$	gamma function with argument $z$ , $=\left(\int_0^\infty t^{z-1} e^{-t} dt\right)$
$Q_k$	water flow rate associated to a $k$ -trajectory, m <sup>3</sup> /s	$\mu, \mu_t$	continuous-phase molecular and turbulent dynamic viscosities, Pa s
$Re_d, Re_t, Re_z'$	Reynolds number for drop phase; high turbulence Reynolds numbers	$\dot{\eta}$	number flow rate of drops, s <sup>-1</sup>
$S$	source term for momentum-transfer interaction between the drops and the air, m/s <sup>2</sup>	$\pi$	constant, 3.141592654
$\Delta t, t$	time interval; time, s	$\rho, \rho_d$	continuous-phase density; discontinuous-phase density, kg m <sup>-3</sup>
$u, u_{z,o}, u_{z,t}$	velocity of the discontinuous phase (drops); initial $z$ -velocity component of drop in the mixing chamber; terminal velocity of drops and drop velocity at nozzle orifice, m/s	$\sigma$	surface tension, N m <sup>-1</sup>
$U$	velocity of the continuous phase (air), m/s	$\sigma_g$	dispersion parameter from Log-Normal distribution, Eq. (15).
$\nu_d$	volume of a drop, m <sup>3</sup>	$\sigma_k, \sigma_\varepsilon$	laminar and turbulent Schmidt numbers for $k$ and $\varepsilon$
$V$	volume frequency of drops with diameter $d_d$ , Eq.16; or volume of water collected in each cell of the patternator, Eq. (1), m <sup>3</sup>	Subscripts	
$w, W$	water-impact flux, L/m <sup>2</sup> s; water-flow rate, L/s	$amb$	ambient conditions, $P=86$ kPa, $T=25$ °C
$We_{zs}$	impinging droplet Weber number	$av$	average
$x, y, z$	rectangular coordinates, m	$cell$	discretization cell
$x_o, u_o$	vectors of position and velocity for drops at each port of the nozzle orifice, m and m/s, respectively	$comp$	computed by the model
		$d$	drop
		$exp$	measured in laboratory experiments
		$i, j$	indexes for coordinate directions
		$k$	index for port trajectories
		$max$	maximum
		$o$	orifice
		$T$	total number
		$x, y, z$	coordinate directions or indexes for vector components

Superscripts

$o, n$  indexes to indicate output to control volume

## References

- [1] J. E. Camporredondo S., A. H. Castillejos E., F. A. Acosta G., E. P. Gutierrez M., and M. A. Herrera G. *Metallurgical and Materials Transactions B*, 35B:541–560, 2004.
- [2] M. S. Jenkins, S. R. Story, and R. H. Davies. *Proc. 19th Australasian Chem. Eng. Conf., CHEMECA 91*, pp. 1–10, Newcastle, New South Wales, Australia, September 1991.
- [3] J. J. Montes R., A. H. Castillejos E., F. A. Acosta G., E. P. Gutierrez M., and M. A. Herrera G. *Canadian Metallurgical Quarterly*, 47(2):187–204, 2008.
- [4] A. H. Castillejos E., M. A. Herrera G., F. A. Acosta G., R. Santos P., E. P. Gutierrez M., and R. Gonzalez de la P. *2005 McMaster Iron and Steelmaking Symposium 'Thinner Slab Casting'*, pp. 47–58, Hamilton, Ontario, Canada, June 2005.
- [5] C. O. Pedersen. *Int. J. Heat Mass Transfer*, 13(2):369–380, 1970.
- [6] K. Araki and A. Moriyama. *Trans. ISIJ*, 21:583–590, 1981.
- [7] L. H. J. Wachters and N. A. J. Westerling. *Chem. Eng. Sci.*, 21:1047–1056, 1966.
- [8] S. C. Yao and K. Y. Cai. *Exp. Therm. Fluid Sci.*, 1:363–371, 1988.
- [9] J. D. Bernardin, C. J. Stebbins, and I. Mudawar. *Int. J. Heat Mass Transfer*, 40(2):247–267, 1997.
- [10] G. E. Cossali, M. Marengo, and M. Santini. *Int. J. Heat and Fluid Flow*, 29:167–177, 2008.
- [11] J. Schmidt and H. Boye. *Chem. Eng. Technol.*, 24(3):255–260, 2001.
- [12] F. Puschmann and E. Specht. *Exp. Therm. Fluid Sci.*, 28:607–615, 2004.
- [13] L. Bendig, M. Raudensky, and J. Horsky. *78th Steelmaking Conference Proceedings*, pp. 391–398, Warrendale, PA, U.S.A., April 1995.
- [14] H. Fujimoto, N. Hatta, H. Asakawa, and T. Hashimoto. *ISIJ International*, 37(5):492–497, 1997.
- [15] N. Hatta, H. Fujimoto, R. Ishii, and J. I. Kokado. *ISIJ International*, 31:53–61, 1991.
- [16] N. Hatta, H. Fujimoto, and R. Ishii. *ISIJ International*, 31:342–349, 1991.
- [17] R. J. Issa and S. C. Yao. *J. Thermophys. Heat Transfer*, 19:441–447, 2005.
- [18] M. Ciofalo, A. Caronia, M. Di Liberto, and S. Puleo. *Int. J. Heat Mass Transfer*, 50:4948–4966, 2007.
- [19] I. Hernandez C., F. A. Acosta G., A. H. Castillejos E., and J. I. Minchaca M. *Metallurgical and Materials Transactions B*, 39B:746–763, 2008.
- [20] Oxford Lasers Imaging Division. Visisizer system manual. Technical Report Issue 1 rev 2, Oxford Lasers Ltd, 2008.
- [21] I. G. Bowen and G. P. Davies. Technical Report ICT 28, Shell Research Ltd., London, 1951.
- [22] C. T. Crowe, M. P. Sharma, and D. E. Stock. *J. Fluids Eng.*, 99:325–332, 1977.
- [23] C. R. Yap. *Ph.D. Dissertation*. University of Manchester, Manchester, UK, 1987.
- [24] E799-92 (Reapproved 1998): Standard Practice for Determining Data Criteria & Processing for Liquid Drop Size Analysis. '2000 Annual Book of ASTM Standards. General Methods & Instrumentation. Volume 14.02. pp. 343–347'.
- [25] R. A. Mugele and H. D. Evans. *Industrial and Engineering Chemistry*, 43(6):1317–1324, 1951.
- [26] A. H. Lefebvre. *Atomization and Sprays*, pp. 367–405. Taylor & Francis Group, Boca Raton, FL, 1989.